

# A Synthetic Case Study of Measuring the Misfit between 4D Seismic Data and Numerical Reservoir Simulation Models through the Momenta Tree

Aurea Soriano-Vargas<sup>a</sup>, Klaus Rollmann<sup>a</sup>, Forlan Almeida<sup>b,d</sup>, Alessandra Davolio<sup>b</sup>, Bernd Hamann<sup>c</sup>, Denis J. Schiozer<sup>b</sup>, Anderson Rocha<sup>a</sup>

<sup>a</sup>*Institute of Computing, University of Campinas*

<sup>b</sup>*Center for Petroleum Studies, University of Campinas*

<sup>c</sup>*Department of Computer Science, University of California, Davis, U.S.A.*

<sup>d</sup>*Engineering Center, University of Pelotas*

---

## Abstract

Data assimilation is an important and time-consuming process in petroleum reservoir numerical simulation. It produces a set of calibrated models used to forecast and optimize oil and gas production. The process focuses on reducing uncertainties related to reservoir properties, yielding numerical reservoir models that plausibly reproduce measured data from the field, such as well rates and pressure.

Besides the traditional well-production data, 4D seismic data are increasingly being used to reduce the uncertainty of numerical reservoir models, by providing dynamic spatial data to be matched. Although 4D seismic data reveal essential information about the dynamic behavior of the reservoir, its integration in data assimilation procedures is challenging, especially in a quantitative way, because of their noisy and uncertain nature and their larger resolution when compared to the resolution of simulated data from numerical reservoir models.

The development of metrics able to efficiently estimate the discrepancies between 4D seismic data and numerical reservoir model outputs is a current research interest for data assimilation, given the challenges of integrating these different types of data.

We introduce the Momenta Tree. It uses orthogonal moments supporting a multi-level data representation, where features are organized in nodes related to different levels of region detail. It supports the comparison of simulated data from numerical reservoir models and observed 4D images of seismic data, images, using different resolutions and considering various domains. The similarity between

---

\*Corresponding author: Aurea Soriano-Vargas. All authors collaborated on all aspects of the work and in the manuscript presented here. ASV: code and benchmark development, and manuscript preparation; KR: color mapping; FA, AD: real case data and result interpretation; DS: petroleum result supervision; BH: image processing methodology and design supervision; AR: study planning and supervision. ASV drafted the manuscript, and the other authors commented on each draft.

*Email addresses:* aurea.soriano@ic.unicamp.br (Aurea Soriano-Vargas), klausr3s@gmail.com (Klaus Rollmann), forlan@cepetro.unicamp.br (Forlan Almeida), davolio@cepetro.unicamp.br (Alessandra Davolio), hamann@cs.ucdavis.edu (Bernd Hamann), denis@cepetro.unicamp.br (Denis J. Schiozer), anderson.rocha@ic.unicamp.br (Anderson Rocha)

data is calculated with the extended Jaccard distance and is represented by a phylogenetic tree; the simulated models are represented as circles in branches, and their similarity is captured by connections. We apply the Momenta Tree to a controlled case, introduced in this paper, to validate and compare the new metric with traditional metrics, and a more complex representative case based on real oil industry data.

Our results show that the Momenta Tree metric retains the same sequential similarity in environments affected by noise. **The highest-ranked models using the Momenta Tree relate to forecast behavior closer to the reference data than the highest-ranked models obtained with traditional methods. An additional advantage of the Momenta Tree is its ability to enable data comparison in various domains (P-impedance and Water Saturation) at different resolutions of seismic and simulation data.**

*Keywords:* Similarity, 4D Seismic Assimilation, Data Assimilation, Visual Data Analysis, Numerical Reservoir Simulation

---

## 1. Introduction

Lack of information complicates the generation of reliable numerical reservoir models of oil and gas fields [1, 2]. Usually, initial scenarios exhibit results far from those observed in the production unit (measured data). Data assimilation improves the predictive capabilities of reservoir models by  
5 updating rock and fluid properties constrained by field data.

Traditional data assimilation procedures use well production data, i.e., fluid rates and pressure. While these data are highly frequent, they are spatially sparse for a petroleum field. Time-lapse or 4DS is employed as an additional source of data to be assimilated [3, 4, 5, 6]. 4DS data complement well data with the potential to provide rich spatial information but at years apart during production.  
10 Under adequate conditions, 4DS data provide information about dynamic reservoir changes, such as fluid saturation, pressure, and other data relevant to field management and production optimization.

Although the use of 4DS data to manage petroleum reservoirs increased in the last decade, assimilation with other data remains challenging [2, 7] and its use remains mostly qualitative. Its quantitative use requires robust metrics to measure the discrepancy with the reservoir simulation  
15 model predictions.

Some methods define the difference between the pixel values of the simulation models and corresponding seismic data with the mean-squared error (MSE) [8, 9], defined by Equation 1.

$$MSE(A, B) = \frac{1}{n} \sum_{i=1}^n (A_i - B_i)^2, \quad (1)$$

where  $A$  and  $B$  are matrices,  $n$  is the number of elements in each matrix, and  $A_i$  and  $B_i$  are the values in position  $i$ .

However, these methods may be insufficient to deal with some important problems: (i) the comparison between models is simplified to the sum of differences between pixels; (ii) the horizontal resolution of simulation model output is smaller than the set of seismic attributes, and; (iii) comparing data from various domains in a traditional approach requires the data to be converted to a common domain.

In this context, we introduce the Momenta Tree to compare simulated data from numerical reservoir models to observed 4DS data. This metric uses seismic and reservoir simulation models as bidimensional images and can compare data at different resolutions and in various domains, in environments affected by noise. The key concept is the representation of the model/seismic images as trees of relevant characteristics related to image regions. A distance matrix is obtained by evaluating pairs of trees. Finally, a phylogenetic tree<sup>1</sup> is obtained, representing the similarity between images, where each image is represented as a circle and the similarity as the ancestry relationships. Our strategy outperforms pixel-wise comparison methods in different scenarios such as when considering different domains, dynamic environments with changes in the analyzed maps and when noise is present.

Prior work lacks a coherent set of standard synthetic data to evaluate similarity. Most authors employ binary shapes representing isolated anomalies to evaluate results [10, 11], but these figures do not represent characteristics of the real reservoirs. When a map is binarized, subjective choices must be made, e.g., one must choose the appropriate break threshold. In addition, and as a consequence, one loses the more gradual changes in values across the map, affecting the similarity between models. For that reason, we introduce a benchmark to evaluate similarity, defined as incremental, controlled synthetic perturbations from seismic data. We aim to generate new images (model/seismic) with a known incremental variation so that each image has a sequential similarity to the first image.

The paper is organized as follows. In the next section, we discuss related work. Section 3 provides an overview and description of the methodology for the Momenta Tree. Section 4 describes the benchmark used. Section 5 presents the application of the methodology to two cases: a synthetic controlled case and a realistic case for comparison of simulated data from numerical reservoir models to observed 4DS data inspired by the hypothesis of a satisfactory match would increase our confidence in a correct understanding of the reservoir behavior. We conclude the paper and discuss future work in Section 6.

## 2. Related Work

Most approaches for integrating 4DS data into assimilation problems are typically performed in the elastic attributes domain, usually acoustic impedance [12]. Other possibilities are the seismic

---

<sup>1</sup>A diagram that represents evolutionary relationships among elements.

amplitude domain and the pressure and saturation domains (engineering domains) [13, 14]. Forward-  
50 modeling or seismic inversions are necessary, which makes data integration challenging. Running seis-  
mic inversions to estimate elastic changes (or even pressure and saturation changes) is time-consuming  
and leads to issues to be handled, such as multiple solution and model uncertainties. Forward-modeling  
to generate seismic amplitude is also time-consuming even if we use the 1D convolution approach. For  
instance, a demanding step is the grid transference (for the stratigraphic reservoir model grid to a reg-  
55 ular seismic volume) needed for every simulation model run in a data assimilation procedure (usually  
thousands of models). Recent efforts propose to compare data in different domains to avoid such  
procedures and simplify data comparison [15, 16].

Even with images in the same domain, comparing distinct data is not trivial [8, 9]. This issue was  
also explored in other contexts, for example, to reduce the number of models and/or select the most  
60 reliable ones [17, 18, 19].

Some approaches convert seismic images into a binary representation to capture main characteris-  
tics of the images and apply a pixel-wise comparison [20], with particular focus on Hamming distance  
[21], Hausdorff distance [22, 23], or a Hausdorff distance modification, called a local dissimilarity map  
[8, 9, 15], which is still a pixel-wise approach but considers a local neighborhood.

65 Some authors use metric-space approaches to convey the similarity between data using a distance  
function. Both types of data (4DS data and numerical reservoir models) are represented as points  
in the metric spaces, where the distance between two points indicates how similar they are. Suzuki  
and Caers [17] proposed the use of Hausdorff distance, as a static metric to measure the similarity  
between reservoir models. The similarity space is explored by a stochastic search in a neighborhood-  
70 based algorithm. Scheidt and Caers [18] also used Hausdorff distance to create a dissimilarity matrix,  
comparing all reservoir models. The resulting matrix is designed using multidimensional scaling with  
a kernel method. Rahim and Li [24] explored methods based on probability distance, where an  
optimization problem is solved to find an optimal subset with similar distribution characteristics to  
the entire model set. However, this potentially time-consuming approach may not converge in the  
75 presence of outliers.

Other authors proposed the use of clustering strategies on metric spaces. Scheidt and Caers  
[25] applied a distance-based kernel clustering technique (DKM). DKM defines a dissimilarity matrix  
by using a dissimilarity function, such as Hausdorff distance, to obtain a 2D map of the models  
using multidimensional scaling. Kernel methods are applied to the new space to overcome non-linear  
80 variation of the points. Finally, a clustering method is applied to classify models and select a subset.  
Using a similar strategy, Sahaf et al. [11] evaluated the similarity between models using a new  
measure based on mutual information. The dissimilarity matrix is projected onto a 2D space with

multidimensional scaling techniques. The resulting 2D map is clustered, and centroids are selected as representatives for each cluster.

85 **Although some research is based on the comparison between pixels, recent efforts [26, 27] have used wavelet coefficients to sparsely represent seismic attributes from the perspective of imaging processing.**

Following a different strategy, Rojas et al. [19] proposed the use of machine-learning techniques, by designing a Multilayer Perceptron network, to minimize the loss of realistic geological representations. Realistic relationships between geometric variables are modeled, ensuring that only geologically-  
90 realistic models are history matched.

These approaches are insufficient to compare simulated data from numerical reservoir models to observed 4DS data because of: (i) reliance on global techniques for comparison; (ii) difficult comparisons when using different resolutions or domains; and (iii) oversimplification, such as conversion of models to binary images, causing severe information loss.

### 95 **3. Comparing 4D Seismic Data and Simulated Data from Numerical Reservoir Simulation Models through Momenta Trees**

The rationale for 4DS data integration is that integrating complementary data constrains better the reservoir simulation model [20]. Three important requirements for 4DS assimilation are: (i) efficiency of image comparison of simulated data from numerical reservoir models to observed 4DS data, even  
100 at different resolutions and in various domains; (ii) a metric to capture the similarity of decreasing anomalies; and (iii) a comparison focusing on global and local behavior properties.

Based on these requirements, we propose to use image comparison methods, widely used in the field of computer vision, to analyze the similarity of 4DS data and numerical reservoir models as images, which can be used in conjunction with existing optimization techniques in the data assimilation  
105 process. Figure 1 depicts the proposed methodology. For a given set of models and/or seismic images (Figure 1.a), complete quadtrees of Orthogonal Variant Moments (OVMs) (Figure 1.b) are built capturing the main characteristics of multi-level regions by recursively subdividing the original image into four quadrants. We consider the characteristics of the whole image, but also emphasize the characteristics of each sub-region in the tree structure. A dissimilarity matrix (Figure 1.c) is obtained  
110 by calculating for each position as the sum of the distances of equivalent nodes of the corresponding quadtrees, using the extended Jaccard distance [28]. Finally, the dissimilarity matrix serves as an input to a Neighbor-Joining algorithm [29] for phylogenetic reconstruction. The resulting phylogenetic trees (Figure 1.d) reflect each model/seismic tree as a point and the similarity as the ancestry relationships of trees.

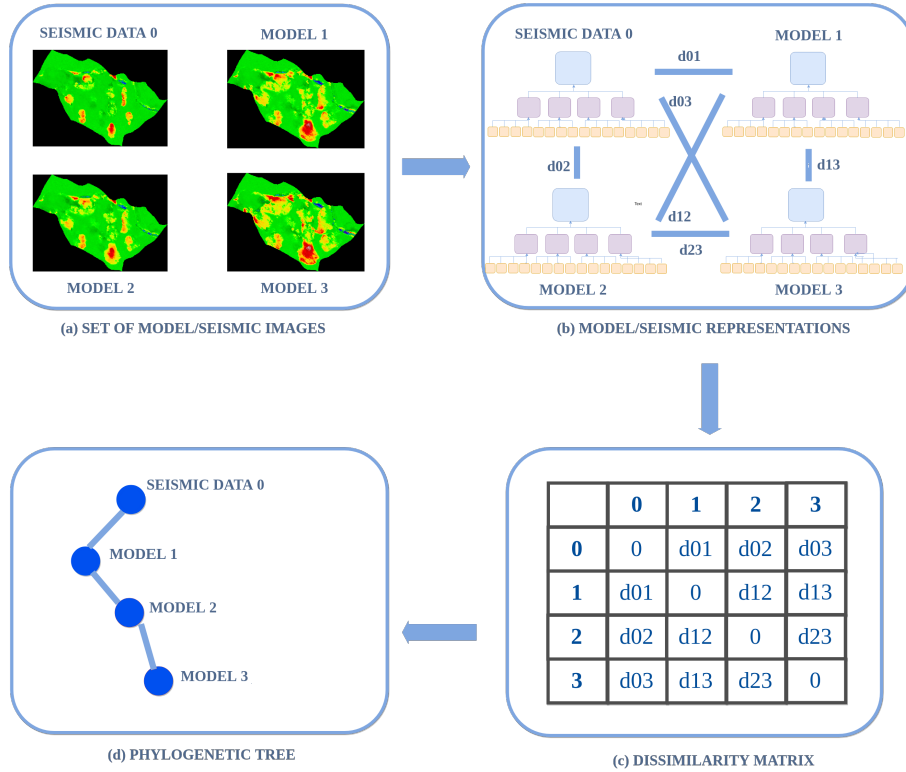


Figure 1: Workflow for the similarity of images from 4DS data and numerical reservoir simulation models. The images (a) are represented as trees of relevant characteristics (b). A dissimilarity matrix is obtained by evaluating pairs of trees (c). Finally, a phylogenetic tree is generated (d) that reflects each model/seismic tree as a circle and similarity as the ancestry relationships of trees.

### 115 3.1. Model Representation

The main characteristics are captured to represent the local descriptive view of each reservoir simulation model or 4DS data [8], further simplifying the analysis. For achieving this, each image is represented as a complete quadtree (also known as tree-pyramid) [30] of main features, as illustrated in Figure 2.

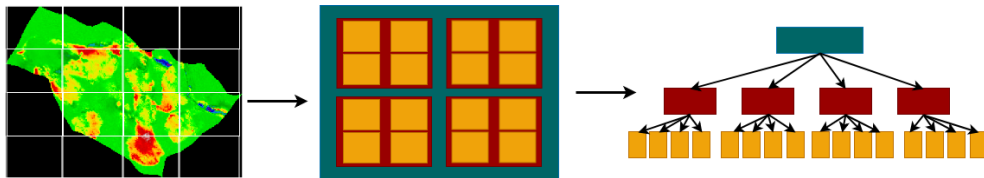


Figure 2: **Image quadrants.** An image is divided into four quadrants in each iteration. OVMs are calculated for each quadrant in each iteration to characterize each one; they are stored in the Momenta Tree nodes.

120 This representation allows recursively decomposing an input image into four quadrants and storing features of each quadrant as nodes of the tree. The vector of features of larger quadrants are stored

in nodes at a higher level of the tree hierarchy, and features of smaller quadrants are at lower levels. We rely on Orthogonal Variant Moments (OVM) [31] to obtain relevant information about a certain quadrant.

125 The OVM features consider the images as a surface, as shown in Figure 3. With this strategy, the comparison is based on the shapes, sizes, and positions of the anomalies.

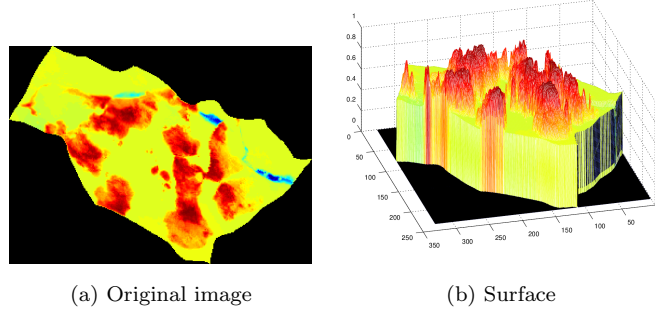


Figure 3: OVM features represent the images as surfaces.

The resulting feature vector consists of seven moments, considering a normalization factor

$$\eta = \frac{1}{h \times w}, \quad (2)$$

where  $h$  and  $w$  are image height and width, i.e., the numbers of image rows and columns, respectively.

The first moment is the area, which is the sum of the intensities of all pixels, also known as the zeroth order moment  $M_{00}$ :

$$A = \eta \int \int f(x, y) dx dy. \quad (3)$$

The second and third moments are defined as the orthogonal components  $L_x$  and  $L_y$ , defined as

$$\begin{aligned} L_x &= \eta \int \int \sqrt{1 + \left(\frac{\partial f}{\partial x}\right)^2} dx dy, \\ L_y &= \eta \int \int \sqrt{1 + \left(\frac{\partial f}{\partial y}\right)^2} dy dx. \end{aligned} \quad (4)$$

The fourth and fifth moments define a unique position, similar to the center of mass concept, i.e.,

$$\begin{aligned} D_x &= \eta \int \int (x + dx) f(x, y) dx dy, \\ D_y &= \eta \int \int (y + dy) f(x, y) dy dx. \end{aligned} \quad (5)$$

The sixth and seventh moments are related to time derivatives, i.e., velocity and acceleration, defined as

$$\begin{aligned}\bar{V} &= \left( \frac{\partial D_x}{\partial t}, \frac{\partial D_y}{\partial t} \right), \\ \bar{A} &= \left( \frac{\partial^2 D_x}{\partial^2 t}, \frac{\partial^2 D_y}{\partial^2 t} \right).\end{aligned}\tag{6}$$

130

For instance, the OVM vector for the matrix in Figure 4 is: [16, 0.98, 0.98, 25.56, 43.64, 8.33, 8.33].

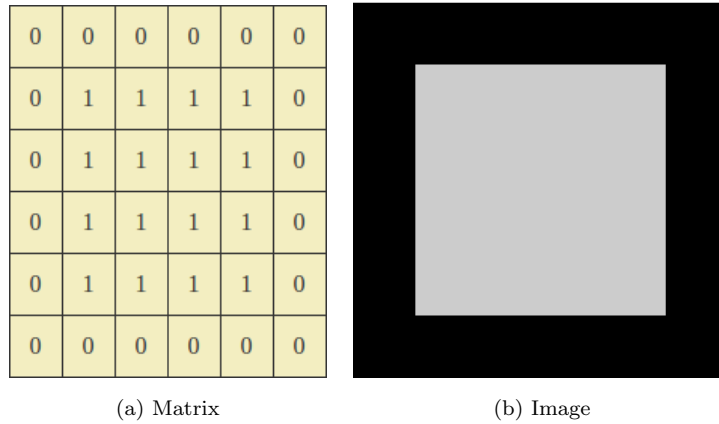


Figure 4: Each matrix is represented as a bidimensional image. The OVM vector for this image is: [16, 0.98, 0.98, 25.56, 43.64, 8.33, 8.33].

Invariant moments are statistical measures commonly used to extract texture information from images [32]. Traditional invariant moments extracted from similar shapes remain the same, even  
 135 when applying geometric transformations. In the 4DS data context, it is necessary to capture small perturbations and changes such as rotation, scaling, translation, and/or contrast, i.e., to measure small transformations in an image. We selected the **OVMs** to represent each image region; these moments measure a transformation; they are not invariant to it. If a specific perturbation occurs, it is measured. This strategy, using complete quadtrees combined with OVMs, allows images to be  
 140 compared at different resolutions through the evaluation of corresponding levels in the tree.

### 3.2. Measuring the Dissimilarity between Reservoir Models and 4D Seismic Data

For creating the dissimilarity matrix, pairs of quadtrees are compared by computing the sum of the dissimilarity of equivalent nodes (same positions in the same tree level) using the extended Jaccard coefficient [33], see Equation 7.

145 As data may have different resolutions, i.e.,  $234 \times 326$  blocks for seismic data and  $58 \times 81$  blocks for simulation data, the images may have different sizes (height and width). In this case, their respective quadtrees will have different depth levels.

For comparison, we calculate the sum of the results of the extended Jaccard coefficient applied to equivalent nodes of both trees. In the example shown in Figure 5, a comparison is made up to the third level in yellow, since there are no nodes on the left equivalent to the nodes in green. We define the distance of quadtrees as

$$d(A, B) = \sum_{a \in A, b \in B}^{\min(L_A, L_B)} jaccard(a, b), \quad (7)$$

$$jaccard(a, b) = \frac{a \cdot b}{\|a\|_2^2 + \|b\|_2^2 - a \cdot b},$$

where  $A, B$  are complete quadtrees,  $a$  and  $b$  are nodes in  $A$  and  $B$ , respectively, and  $L_A$  and  $L_B$  are the maximum depths of  $A$  and  $B$ .

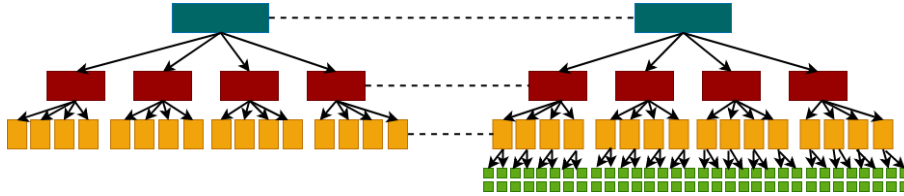


Figure 5: Quadtrees of orthogonal Variant moments are compared by computing the sum of extended Jaccard coefficients of equivalent nodes. Here, comparisons are performed until the third level (yellow).

### 3.3. Phylogenetic Trees of Reservoir Models and 4D Seismic Data

155 Phylogenetic trees are diagrams to represent the connections of biological species linked in the past by common ancestors [34]. We use phylogenetic tree representation to obtain a visual similarity map from the dissimilarity matrix. One main advantage of the phylogenetic tree is its simplicity for visual understanding [35].

To generate phylogenetic trees from a dissimilarity matrix, we use the Neighbor-Joining (NJ) technique proposed by Cuadros et al. (2007) [29], which has been applied to biological and non-biological datasets, including text and images. This technique relies on a tree hierarchy, where elements of the dissimilarity matrix are shown as leaf nodes, and virtual nodes (internal) are created to join similar points, considered hypothetical ancestors for these nodes. In our application, each leaf node represents a reservoir model or a 4DS data set. Edges (connections) between nodes represent the similarity, while path distances represent the dissimilarity proportionally. Nodes may contain up to three branches, one node connected to the ancestor node and the other two nodes connected to the

165

two most similar nodes. Rotating the similar nodes does not change their relationship, as Figure 6 illustrates.

The technique begins with a star tree because pairs of elements have not been grouped yet. The first pair of elements to be grouped is chosen, applying the minimum evolution criterion, which attempts to minimize the sum of the sizes of all nodes in the tree. The selected elements have the lowest value in the calculation of the sum of the distances between branches, considered as neighbors. We use the equation

$$S_{ij} = \frac{1}{2(n-2)} \sum_{k \neq i,j}^n (D_{ik} + D_{jk}) + \frac{1}{2} D_{ij} + \frac{1}{n-2} \sum_{(k,l \neq i,j) \wedge (k < l)}^n D_{kl}, \quad (8)$$

where  $D_{ij}$  is the value in the distance matrix, and  $n$  is the number of elements.

Once the pair of neighboring elements to be grouped in a new virtual node  $X$  has been chosen, the sizes of new branches are calculated by the Fitch-Margoliash method using the equations

$$\begin{aligned} L_{iX} &= \frac{D_{ij} + D_{iz} D_{jz}}{2}, \\ L_{jX} &= \frac{D_{ij} + D_{jz} D_{iz}}{2}, \end{aligned} \quad (9)$$

where  $z$  is the group of elements, except objects  $i$  and  $j$ .  $D_{iz}$  and  $D_{jz}$  are the distances of elements  $i$  and  $j$  to all other elements, i.e.,

$$\begin{aligned} D_{iz} &= \frac{\sum_{k \neq j}^n D_{ik}}{n-2}, \\ D_{jz} &= \frac{\sum_{k \neq i}^n D_{jk}}{n-2}. \end{aligned} \quad (10)$$

The new virtual node  $X$  replaces the elements  $i$  and  $j$  in the matrix. Consequently, elements  $i$  and  $j$  are removed from the matrix, and the distances from the virtual node and the other nodes are calculated as

$$D_{i-j,k} = \frac{D_{i,k} + D_{j,k}}{2}, \quad (11)$$

170 where  $k \leq n$ , not including  $i$  and  $j$ .

At each iteration, the number of elements is reduced by one unit up to three elements.

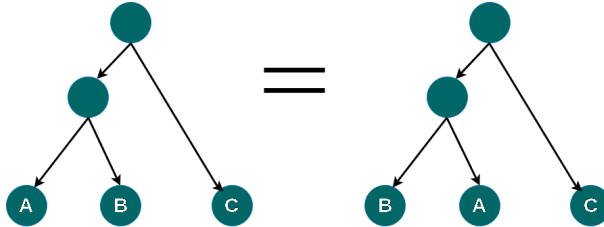


Figure 6: Rotating similar nodes does not change their relationship.

The resulting phylogenetic tree can be interpreted as follows:

1. Each simulation model is placed on the visualization as a colorful circle and the seismic as a black circle.
- 175 2. The color of each model represents the quality related to the selected objective functions.
3. The distance denotes the level of similarity in relation to the comparison used.
  - Models that are more similar to each other are placed closer, even on the same branch.
  - Models that are more different are placed in distant places (different branches).
4. The models most similar to seismic will be found in the same branch of seismic.
- 180 5. The model that is closest to seismic on the same branch will be the most similar model.
6. If we find well-formed branches containing circles with similar colors, they will represent a set of similar scenarios in terms of well matching and spatial fluid similarity.

We wish to emphasize the novel components of our approach: (i) a consistent representation of the main characteristics of different regions, capable of identifying any variation; (ii) a simplified  
185 dissimilarity comparison that allows the comparison of images of different sizes; and (iii) a general dissimilarity visualization that allows the efficient evaluation of similarity between reservoir simulation models and 4DS data.

#### 4. Benchmark

We use a benchmark case, UNISIM-I<sup>2</sup>, as our base dataset to evaluate our methodology. The  
190 benchmark is a synthetic black-oil reservoir based on a real field [36]. The synthetic seismic data was obtained through the high-resolution simulation model UNISIM-I-R (234 × 326 blocks), which represents the reference case (true answer). First, a petro-elastic model (PEM) was applied to obtain the elastic attributes from the UNISIM-I-R reservoir model parameters. A seismic forward model (1D convolution) generated seismic traces. Finally, a colored inversion was executed to estimate “observed”  
195 impedance changes.

A petro-elastic model can be defined by forward rules used to compute the elastic properties from studied reservoir properties [37]. Colored inversion is a fast method proposed by Lancaster and Whitcombe (2000) [38] for band-limited inversion of seismic data. Based on the fact that the sparse-spike inversion process can be approximated by a single operator, yielding relative impedance  
200 via simple convolution with the reflectivity data, the authors showed that this operator can be derived from well logs.

---

<sup>2</sup>(available on <https://www.unisim.cepetro.unicamp.br/benchmarks/en/unisim-i/overview>)

In our experiments, we used 4DS data maps of P-impedance changes ( $\Delta IP$ ), estimated from inversions. For more details about the seismic data generation, refer to Davolio and Schiozer (2019) [39], and Souza (2017) [40].

205 We also used a set of 500 maps of  $\Delta S_w$  generated from numerical reservoir models, defined on a relatively coarse grid ( $58 \times 81$  blocks) compared to the reference case, by applying the PEM. All data were made available at four-time production instants: (T1) 7Y2M (2618 days), (T2) 9Y0M (3287 days), (T3) 10Y0M (3652 days), and (T4) 11Y0M (4018 days), where Y means years and M months, considering as baseline  $T_0$  at time zero. Thus, data have two different resolutions:  $234 \times 326$  blocks  
 210 for seismic data and  $58 \times 81$  blocks for simulation data, as observed in Figure 7.

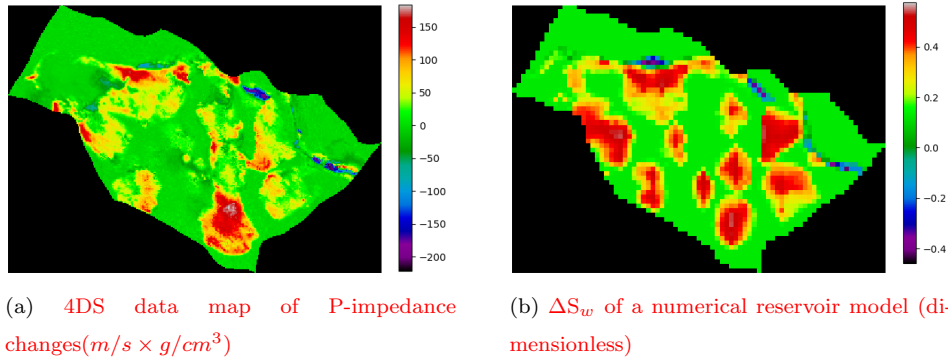


Figure 7: Example of 4DS and numerical reservoir model from T4 (11Y0M - 4018 days).

As there is no absolute response to rank the 500 models or select the best match based on 4DS data, we created controlled perturbations, for which we know the similarity of the samples. To evaluate the workflow, we defined incremental perturbations starting from an ‘observed’  $\Delta IP$  map, normalized using standardization (Z-score normalization). This process generates new reservoir model and/or  
 215 seismic matrices with an incremental variation from normalized ‘observed’ values so that each image had a sequential similarity with respect to the first image. The synthetic perturbations are intended to be consistent with differences that occur between the 500 simulation models and the observed values. These perturbations are related to differences in (i) decreasing size of anomalies regions, (ii) contrast, and (iii) resolution.

220 For the decreasing the perturbation size, we identified the anomalies by separating the image background (green) and foreground (anomalies in yellow/red), using a probability-based approach, assuming that anomalies have lower probabilities than the image background. The fundamental approach calculates the probability of each pixel value, and creates a histogram with 10 bins. The match with the lowest probability is reported as background. Other probabilities are considered  
 225 foreground. Finally, 20 images are created by decreasing the region values of a parameter  $\alpha$ , see

Equation 12. The anomalies are faded out in each iteration.

$$M_i(x, y) = M_{i-1}(x, y) - \alpha, \quad (12)$$

where  $i$  is between 1 and 20,  $M_i$  is the matrix in the range  $i$  based on the normalized observed  $\Delta IP$  map, and  $\alpha = 0.025$ .

For the contrast perturbation, 20 images were created by decreasing each matrix value by means of parameter  $\alpha$ , see Equation 12.

For the resolution perturbation, 20 images were created by decreasing the resolution by 10% of the original grid size, see Equation 13. The resolution was modified but not the image size. The images in Figure 8 present the differences in resolution of 5 of the 20 images,

$$M_r = M_{r-1} - 10\% * M_{r=1}. \quad (13)$$

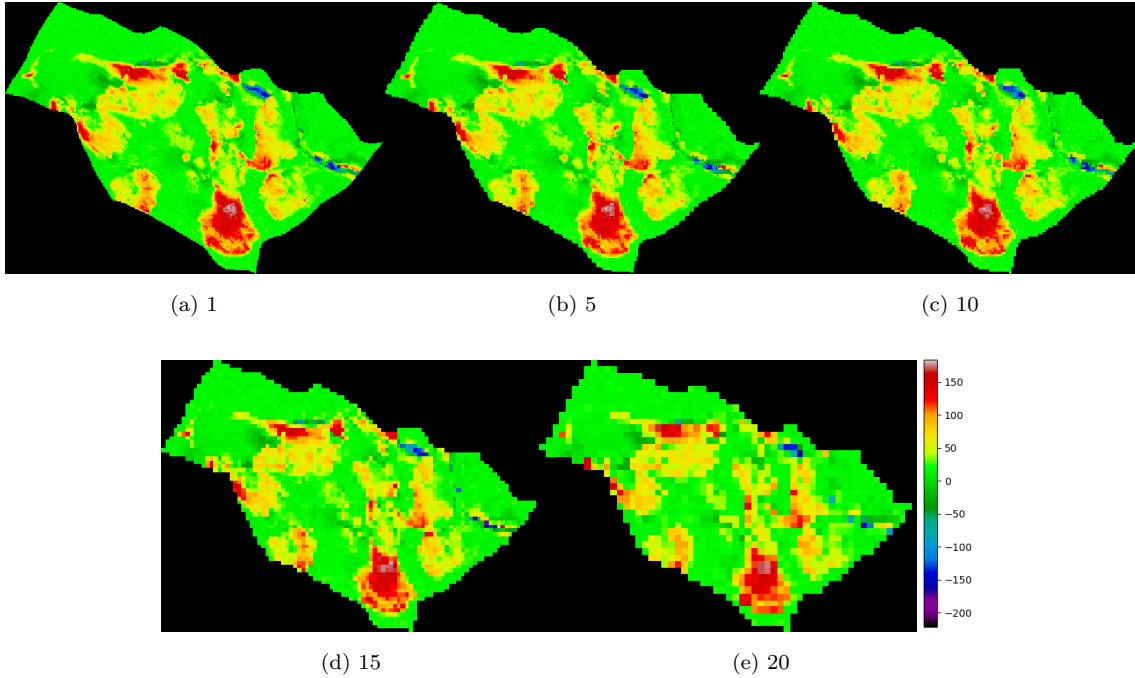


Figure 8: Resolution perturbation for images 1, 5, 10, 15, and 20 based on 4DS data map of P-impedance changes ( $m/s \times g/cm^3$ ).

For evaluation purposes, we used the matrices ‘observed’ at four time production instants ((T1) 7Y2M (2618 days), (T2) 9Y0M (3287 days), (T3) 10Y0M (3652 days), and (T4) 11Y0M (4018 days) as anchors to identify behavior of the ‘observed’ data through time, exploring typical characteristics such as shape, size and position variations. A function  $f_c$  is created per cell  $c \in C$ ,

where  $C$  is the number of cells, considering the cell values  $M_{T_i}(x, y)$  as data points, where  $T_i \in \{T_1:7Y2M, T_2:9Y0M, T_3:10Y0M, T_4:11Y0M\}$ , see Figure 9. Different functions were evaluated using the observed data for the four time instants, such as polynomial functions from degrees two to eight, Lagrange interpolation, cubic spline interpolation, piecewise linear interpolation, and nearest-neighbor interpolation.

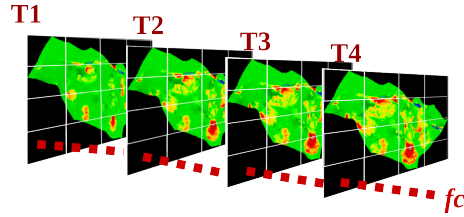


Figure 9: A function  $f_c$  is created per cell  $c \in C$ , where  $C$  is the number of cells, considering the data points as pairs of time instant  $T_i \in \{T_1:7Y2M, T_2:9Y0M, T_3:10Y0M, T_4:11Y0M\}$  and cell value  $M_{T_i}(x, y)$ .

For testing, we created the functions using three of the four time instants  $T_i \in \{T_1:7Y2M, T_2:9Y0M, T_4:11Y0M\}$ , and estimated the values of  $M_{T_3:10Y0M}(x, y)$ , which were compared with the real values of  $T_3:10Y0M$ . We used the average mean-squared error (MSE) to identify the function that best fits the data, by applying it to the corresponding values between the real and the estimated values. Table 1 shows the results.

Interpolation	MSE
Polynomial-2	0.0002094
Polynomial-3	0.0002252
Polynomial-4	0.0002439
Polynomial-5	0.0002661
Polynomial-6	0.0002921
Polynomial-7	0.0003225
Polynomial-8	0.0003580
Lagrange	0.0002094
Cubic Spline	0.0002094
Piecewise Linear	<b>0.0001674</b>
Nearest Neighbor	0.0005661

Table 1: Interpolation functions using three of the four time instants  $T_i \in \{T_1:7Y2M, T_2:9Y0M, T_4:11Y0M\}$ , to estimate the values of  $M_{T_3:10Y0M}(x, y)$  based on 4DS data map of P-impedance changes ( $m/s \times g/cm^3$ ). The obtained and the real values of  $T_3:10Y0M$  were compared using the average mean-squared error (MSE) to identify the function that best fits the data.

We found that the piecewise linear function, which uses simple linear interpolation between data points, results in the lowest average mean-squared error (0.00016). A total of 20 time-lapse synthetic images were created using this strategy at different times between  $T_1$  and  $T_4$ .

## 5. Experiments and Results

250 We explore two case-studies that consider these scenarios: (a) the controlled synthetic perturbations from the provided 4D seismic map, namely a time-lapse difference of seismic impedance ( $\Delta\text{IP\_seis\_obs}_{234\times 326}$ ), related to differences in contrast (20), decreasing anomalies (20), resolution (20), and time-lapse synthetic data (20) obtained by a Piecewise Linear Interpolation and (b) a realistic case: a comparison of 500  $\Delta S_w$  maps of distinguished numerical reservoir models obtained after  
255 well-production data assimilation. We also apply the MSE metric to analyze the similarity of the different datasets, whose results are compared to our strategy results.

### 5.1. Evaluating the Momenta Tree with Synthetic Perturbations

Synthetic perturbations are used to evaluate the ability of the Momenta Tree to characterize variations present in the reservoir models and to test the quality of the method to identify each  
260 variation individually. The images generated from the perturbations are considered as the models to be ranked, i.e., arranged in order by similarity, and the images are classified using the initial image as a reference. The different perturbations emulate the differences between the models and the observed data. The Momenta Tree method must be able to correctly rank the perturbed images and place them in order as they were generated considering different sequential perturbation levels when applied. This  
265 ability is validated when the phylogenetic tree shows nodes in the same order as used to generate the corresponding images.

The Momenta Tree methodology was applied to the 20 images related to the perturbation of decreasing anomalies size. The resulting phylogenetic tree (Figure 10) correctly characterizes the perturbation of decreasing anomalies.

270 The 20 synthetic images related to the variation of contrast were also explored. The resulting phylogenetic tree placed the nodes in the correct sequential order, i.e., the images were placed according to their contrast variations, as shown in Figure 11.

For the 20 images related to incremental variations in resolution, the resulting phylogenetic tree (Figure 12) is not perfectly represented, because the resolution change, which modified the variety of  
275 values, affected the shape and size of the regions.

The 20 time-lapse images, obtained by piecewise linear interpolation, were correctly organized in chronological order, as Figure 13 depicts.

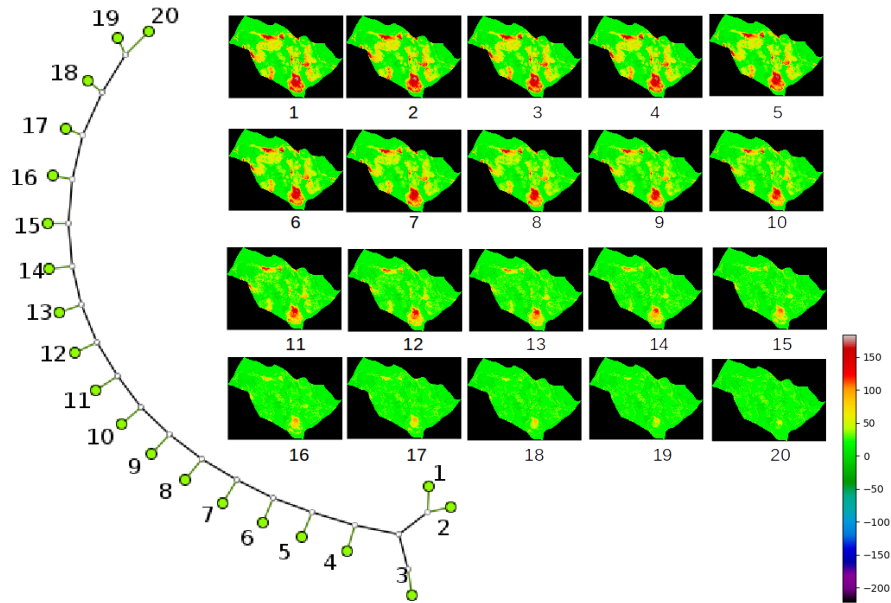


Figure 10: Resulting phylogenetic tree and the 20 images with perturbation of decreasing anomalies based on 4DS data map of P-impedance changes ( $m/s \times g/cm^3$ ). Green circles indicate correct positions and red circles indicate incorrect positions. All positions are correct, therefore no node is marked in red. The results confirm that the strategy perfectly characterized the perturbation of decreasing anomalies.

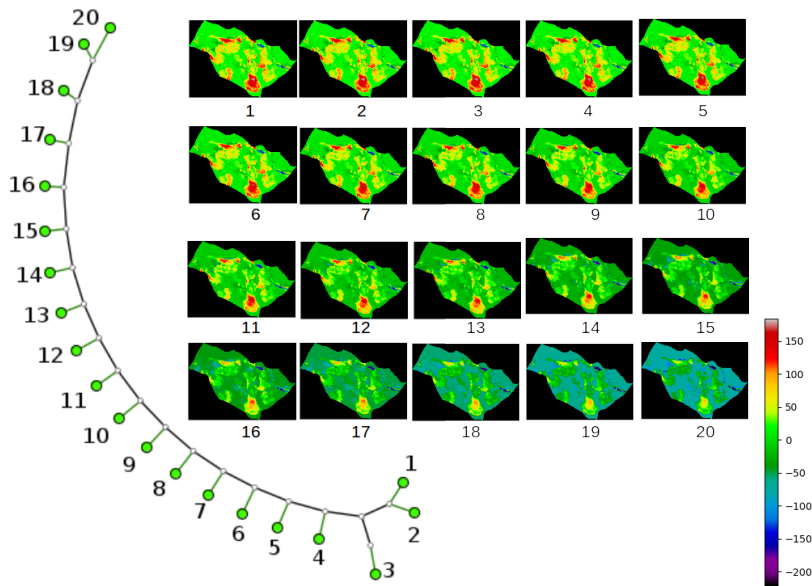


Figure 11: Resulting phylogenetic tree and the 20 images with incremental contrast variation based on 4DS data map of P-impedance changes ( $m/s \times g/cm^3$ ). Edges between nodes represent the similarity, while path distances represent the dissimilarity proportionally. For instance, the phylogenetic tree shows that image 2 is the most similar one to image 1. Green circles indicate correct positions and red circles indicate incorrect positions. All positions are correct, therefore no node is marked in red. These results confirm the correct characterization of contrast using the Momenta Tree.

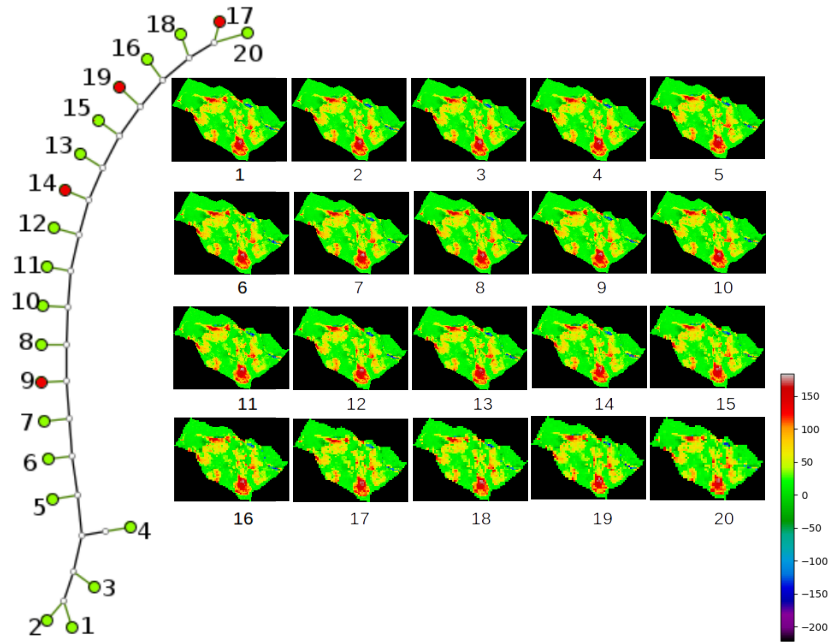


Figure 12: Resulting phylogenetic tree and the 20 images with variation of resolution based on 4DS data map of P-impedance changes ( $m/s \times g/cm^3$ ). Green circles indicate correct positions and red circles indicate incorrect positions. The results show that the variations of resolution were nearly perfectly represented.

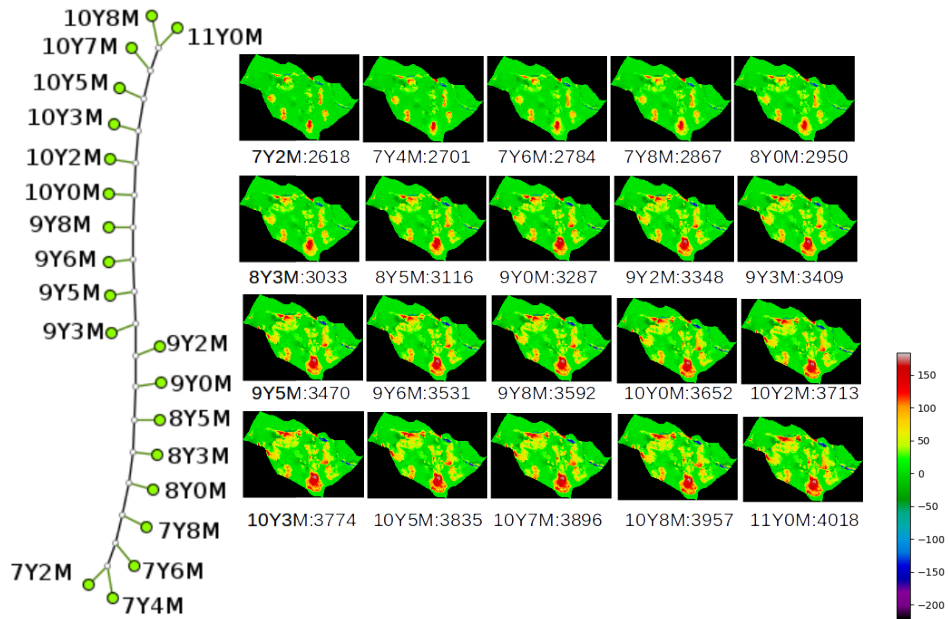


Figure 13: Resulting phylogenetic tree and the 20 time-lapse images using piece-wise linear interpolation based on 4DS data map of P-impedance changes ( $m/s \times g/cm^3$ ). Green circles indicate correct positions and red circles indicate incorrect positions. All positions are correct, therefore no node is marked in red. These results confirm the correct characterization of the linear behavior using the Momenta Tree.

### 5.1.1. Analysis of Noisy Data

We also have investigated the impact of noise in the experiments. We added random noise to the 20 images generated for the contrast perturbation and for the perturbation of decreasing anomalies, using Equation 14.

$$M_c(x, y) = M_{c-1}(x, y) + rand(0, 1) * [max(M_{c-1}(x, y)) - min(M_{c-1}(x, y))], \quad (14)$$

where  $M_c$  is the contrast perturbation matrix,  $rand(0, 1)$  returns a random floating-point number between 0 and 1,  $max(M_c(x, y))$  returns the maximum value, and  $min(M_c(x, y))$  is the minimum value.

The 20 images, obtained by adding noise to both types of perturbation images, were correctly organized in the same sequential similarity arrangement, as Figures 14 and 15 depict.

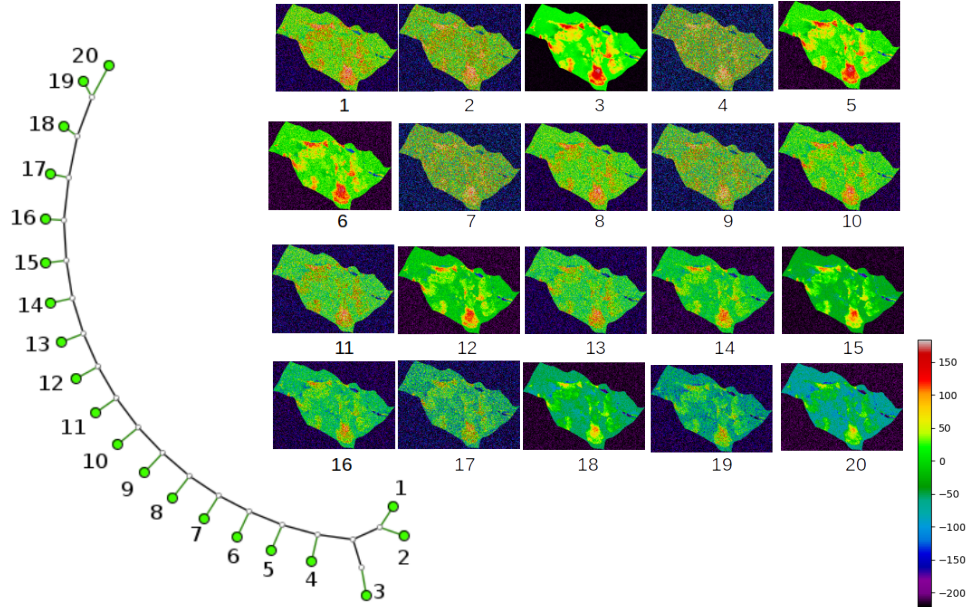


Figure 14: Resulting phylogenetic tree, using MT strategy, and the 20 images obtained by adding noise to the contrast perturbation images. Green circles indicate correct positions and red circles indicate incorrect positions. **All positions are correct, therefore no node was marked in red.** These results confirm the correct characterization of contrast even in the presence of noise.

We also applied the MSE approach to the images with noise, as shown in Figures 16 and 17. The MT strategy retains the same sequence similarity in environments affected by noise; on the other hand, MSE approach is severely affected showing the importance of considering a more robust way of comparing images as we propose in this work.

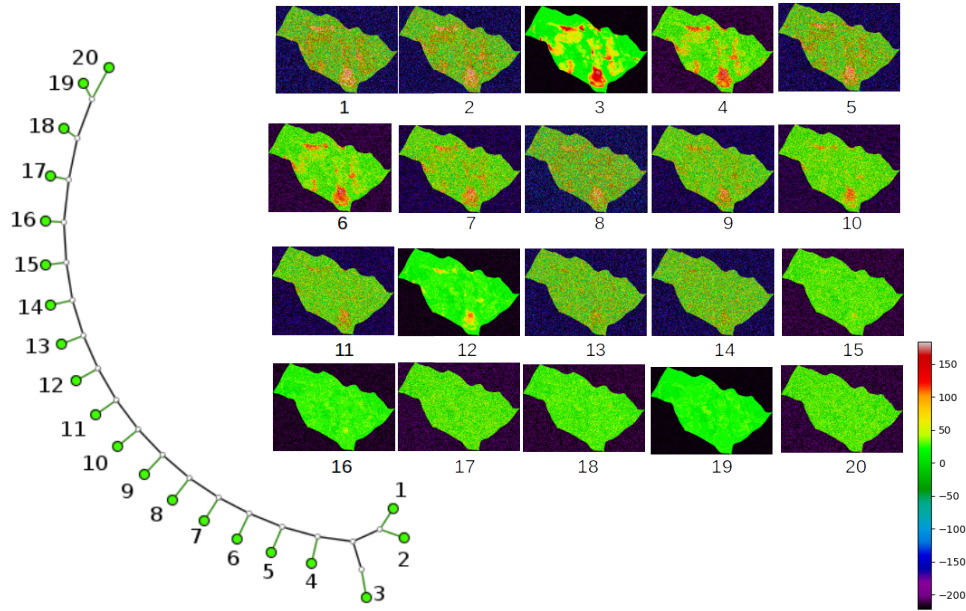


Figure 15: Resulting phylogenetic tree, using MT strategy, and the 20 images obtained ( based on 4DS data map of  $P$ -impedance changes( $m/s \times g/cm^3$ )) by adding noise to the perturbation images of decreasing anomalies. Green circles indicate correct positions and red circles indicate incorrect positions. All positions are correct, therefore no node is marked in red. These results confirm the correct characterization of decreasing anomalies even in the presence of noise.

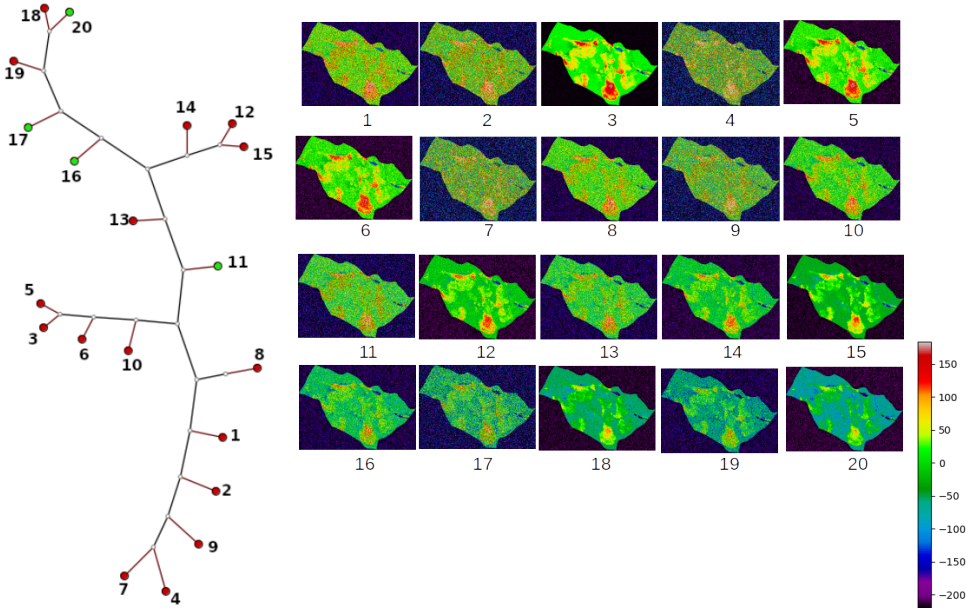


Figure 16: Resulting phylogenetic tree, using the MSE approach, and the 20 images obtained (based on 4DS data map of  $P$ -impedance changes( $m/s \times g/cm^3$ )) by adding noise to the contrast perturbation images. Green circles indicate correct positions and red circles indicate incorrect positions. These results show how the MSE approach is severely affected by noise.

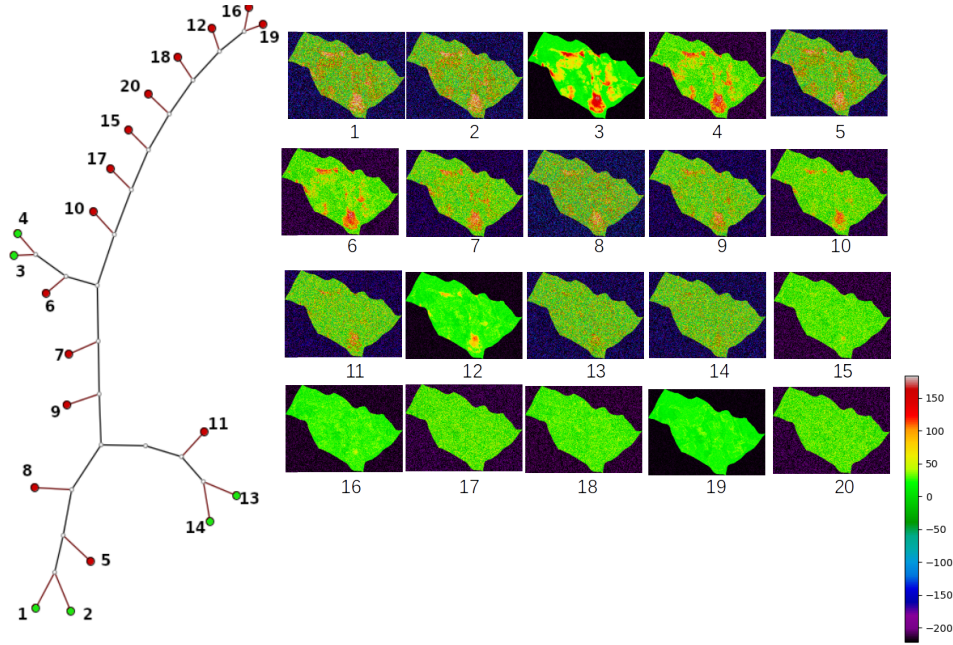


Figure 17: Resulting phylogenetic tree, using the MSE approach, and the 20 images obtained (based on 4DS data map of P-impedance changes( $m/s \times g/cm^3$ )) by adding noise to the perturbation images of decreasing anomalies. Green circles indicate correct positions and red circles indicate incorrect positions. These results show how the MSE approach is severely affected by noise.

### 5.1.2. Discriminatory Power of the Momenta Tree Attributes

With the objective of exploring the discriminatory power of the Momenta Tree attributes, we built a Linear Regression model using the concatenated feature vectors of the Momenta Tree as input and its sequential position as the target variable. For avoiding model evaluation bias, not all the training data were used. We divided the data into two sets: 60% used for training data and 40% used for testing data. We provide an evaluation of our model performance by using the standard error of the estimate, see Equation 15, in the testing data. The standard error of the regression numerically assesses how well a model fits the sample data, i.e., it is an absolute measure of the distances of data points from the regression line.

$$\sigma_{est} = \sqrt{\frac{\sum(Y - Y')^2}{N}}. \quad (15)$$

Here,  $Y$  is the target variable,  $Y'$  the prediction, and  $N$  the number of data points.

We evaluate the Linear Regression models from synthetic perturbation datasets, whose results are shown in Table 2. For instance, a result of 1.87 means a low error of almost two days in a prediction.

Table 2: Standard Error of the Estimation of Synthetic Perturbations

Synthetic Perturbation	Standard Error of the Estimation
Contrast	0.9
Decreasing Anomalies	1.77
Resolution	2.09
Piece-wise Linear	1.87

295 *5.1.3. Comparing MSE Results in Synthetic Perturbations*

We also use the MSE metric, well-used in the related work, for the synthetic perturbations to compare the characterization power of variations. Because of the limitation of pixel-wise comparison, all image sizes must be the same. The similarity results are also shown in phylogenetic trees (Figure 18). MSE captures the sequential variations in contrast, decreasing anomalies, and time-lapse piecewise  
300 linear interpolation. Different resolutions affect the MSE-based comparison of simulated data from numerical reservoir models to observed 4DS data.

*5.2. Seismic  $\Delta IP$  Data versus  $\Delta S_w$  Maps from Simulation Models*

The proposed methodology makes possible the comparison between domains without the need to transform data. Thus, we used the methodology to compare  $\Delta IP$  map (from 4DS data) and 500  $\Delta S_w$   
305 maps extracted from the numerical simulation models. To better analyze the results, we focused on the data comparison in a region around the injector 22 of the case study, see Figure 19. In this case, the 4D anomalies are related to water saturation changes caused by injection. This interpretation has low uncertainty due to the existence of hardening effects, in agreement with the production strategy (surrounding injectors wells). Therefore, this type of comparison is viable. For more complex cases  
310 where competing effects exist and a 4D interpretation is ideally performed with a high degree of reliability, this approach cannot be recommended.

The simulation models used are the results of well-production data assimilation. We measured the quality of the well data matching using the Normalized Quadratic Deviation with Sign (NQDS) metric [36], defined as

$$NQDS = \frac{(\sum_{i=1}^n (Sim_i - Obs_i))}{|\sum_{i=1}^n (Sim_i - Obs_i)|} * \frac{(\sum_{i=1}^n (Sim_i - Obs_i)^2)}{(\sum_{i=1}^n (Obs_i * Tol + C)^2)}, \quad (16)$$

where  $i$  corresponds to a time instant,  $Sim_i$  and  $Obs_i$  are the simulated and observed data measured at time  $i$ ,  $Tol$  is the percentage of tolerance defined by the observed data, and  $C$  is a constant used to prevent division by zero, in case the production rate is zero.

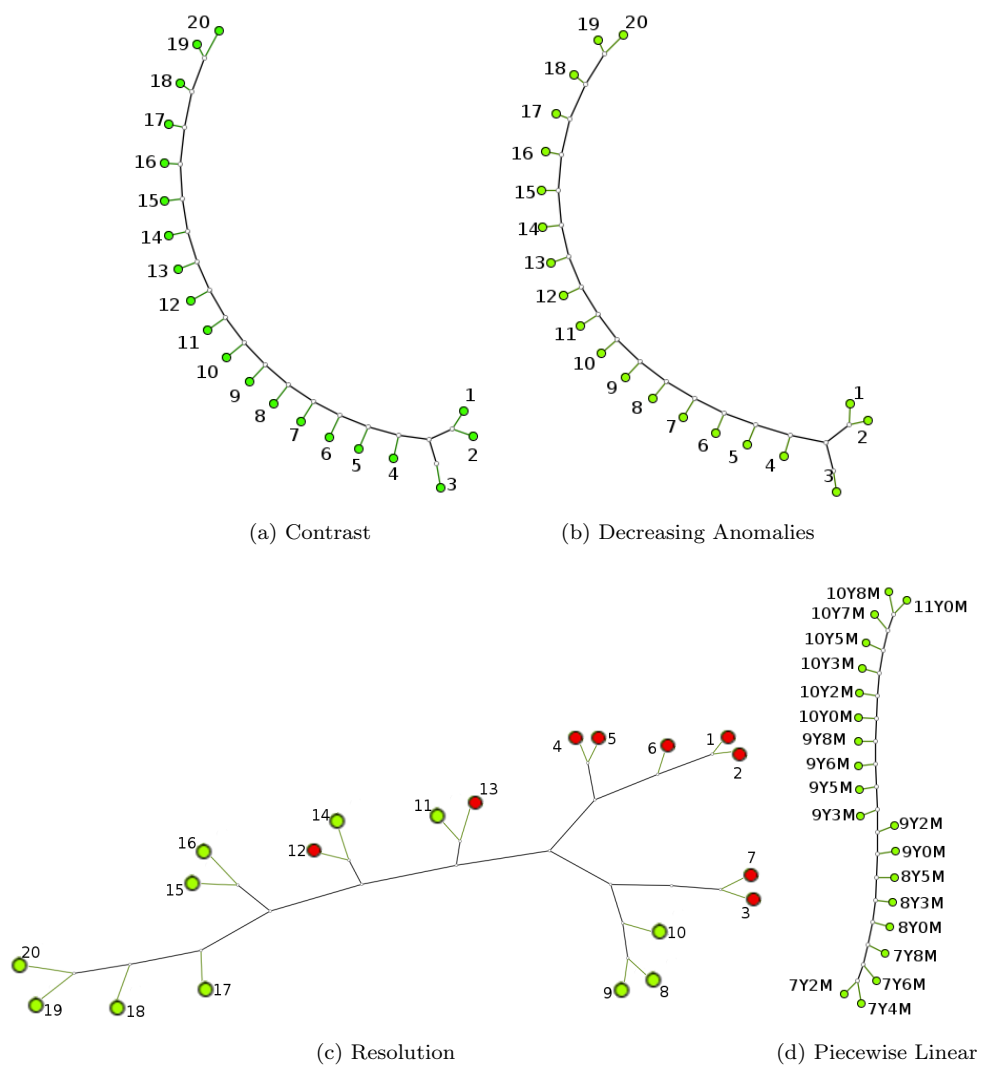


Figure 18: Resulting phylogenetic tree comparing different synthetic perturbations with the MSE technique. Green circles indicate correct positions and red circles indicate incorrect positions. The MSE sequentially captures the variations of contrast, decreasing anomalies and piecewise linear interpolation. The results show the limitations of the MSE approach, not only comparing images of the same size but at the same resolution.

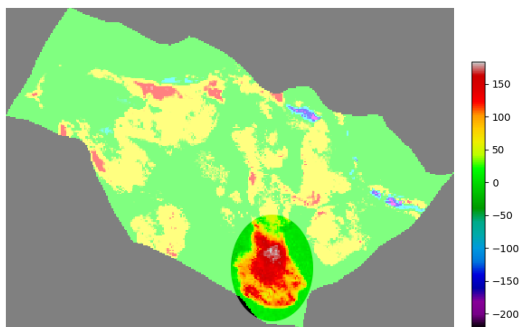


Figure 19: Seismic  $\Delta IP$  map ( $m/s \times g/cm^3$ ) highlighting data belonging to the region around injector 22.

315 As we focus on the region around injector 22 (see Figure 19), we computed the NQDS for Bottom Hole Pressure (BHP) and Water Injection Rate ( $Q_{WI}$ ) of this well. The closer to zero the NQDS value, the higher the similarity between the simulated numerical model data and the historical data. The well-matching quality of each of the 500 models is defined as the maximum absolute value from both NQDS (see Equation 17).

$$color\_index = \max(NQDS\_BHP, NQDS\_Q_{WI}). \quad (17)$$

320

The comparison was performed by generating a phylogenetic tree. As defined in Section 3.3, each model is represented by a colored circle and the 4D seismic data by a black circle. The colors of the circles represent the matching quality of well data based on Equation 17.

325 The distance between circles indicates the similarity of the maps, which can be related to the distance between the  $\Delta S_w$  maps from two models, or the distance between a model and 4DS data.

We generated one phylogenetic tree with the Momenta Tree strategy and another using the MSE, considering the 500  $\Delta S_w$  maps extracted from simulated data of numerical reservoir models, compared to the 4DS data, see Figure 20. These representations show the maps' similarity and also the quality of well history matching for injector 22.

330 The branches of models are conformed by those that have similar distribution of water-related anomalies according to the two different metrics used. Branches in models with similar colors indicate similar models, in terms of water movement and well-data-matching quality. For instance, the models most similar to 4D seismic data, based on MSE, see Figure 20, present poor well matching quality; the Momenta tree metric has identified as most similar models the ones with better well matching.

335 We also chose eight samples of the most similar models (bottom) and least similar models (top) for each strategy. The images were used based on their original resolutions.

To obtain the desired MSE comparison, we used the small transformed resolution of the 4DS

data and normalized the matrices. The Momenta Tree comparison was applied to data of different resolutions and in different domains.

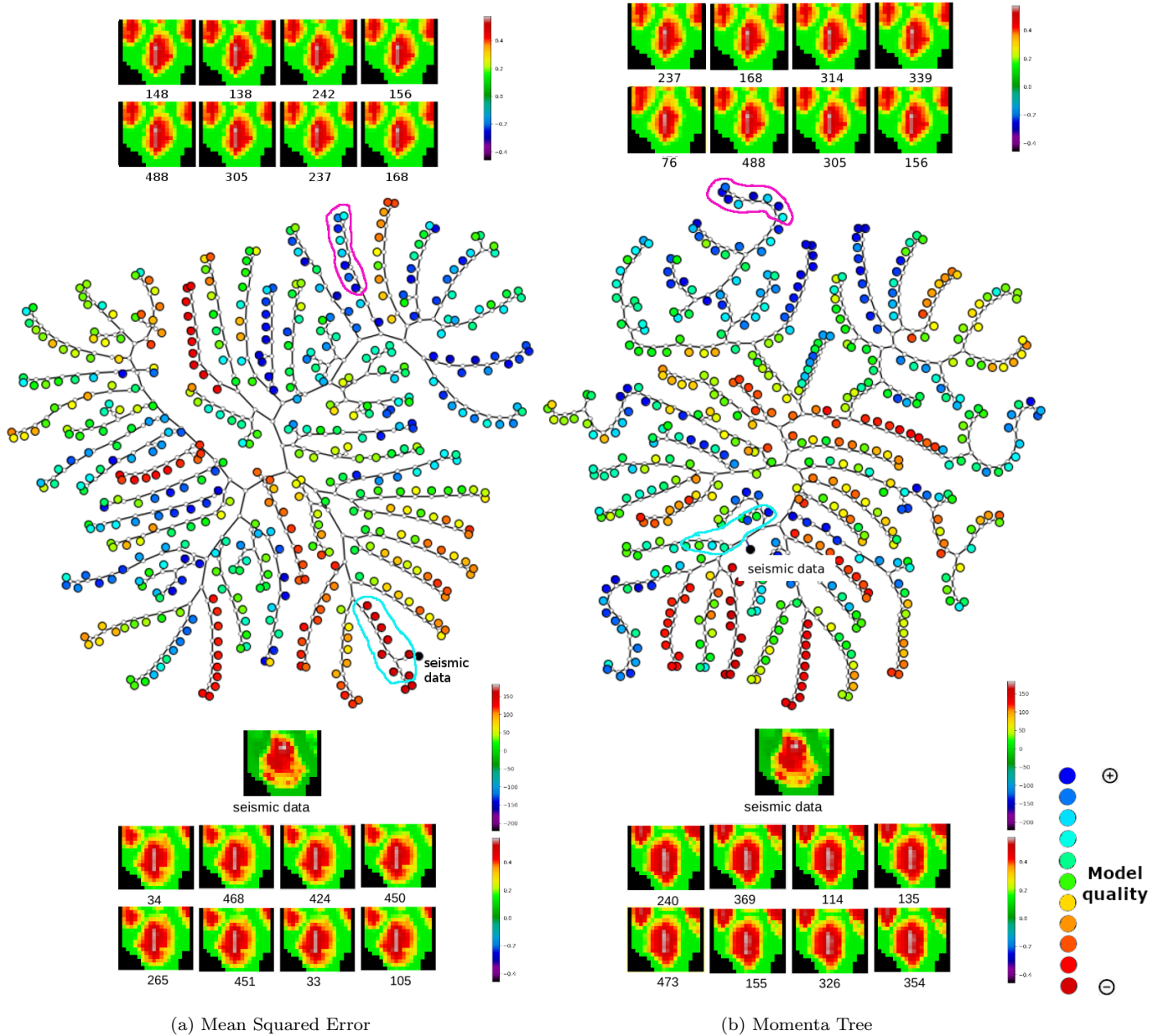


Figure 20: 500  $\Delta S_w$  maps of simulated data (dimensionless) from 500 numerical reservoir models compared with seismic  $\Delta IP$  data ( $m/s \times g/cm^3$ ) using the Momenta Tree and MSE strategies. Blue circles indicate good models, green circles indicate fair models, and red circles imply bad choices related to BHP and  $Q_{WI}$  properties. We also chose eight samples of the most similar models (bottom) and least similar models (top) for each strategy.

as surfaces, observing both general details and specific regions. For this reason, the models found in the top ranking may be a little different.

The results did not indicate which strategy is better for identifying the best fit to seismic data. For that reason, we investigated the 10 (of 500) numerical reservoir models that are closer to the seismic data for both chosen strategies. These models refer to the output of the well data assimilation, using history matching. To rank the best 10 models selected based on their ability to fit 4DS data, using different metrics, we can evaluate the quality of their production forecast.

We explored the local cumulative curves for injector 22 (INJ022), see Figure 21. Evaluating the forecast behavior of water injection from INJ022, the 10 best scenarios selected by the Momenta Tree are closer to the reference behavior than the best 10 scenarios selected by the MSE metric, with the additional advantage of allowing the comparison of data between various domains and at various resolutions. Certainly, reliable forecasts do not depend solely on the metric used to select the 10 models according to 4DS. It is important to consider how the models must be adjusted and how complex the data are. The primary objective is to determine whether the dynamic behavior of the models changes greatly using the MSE metric or the Momenta Tree.

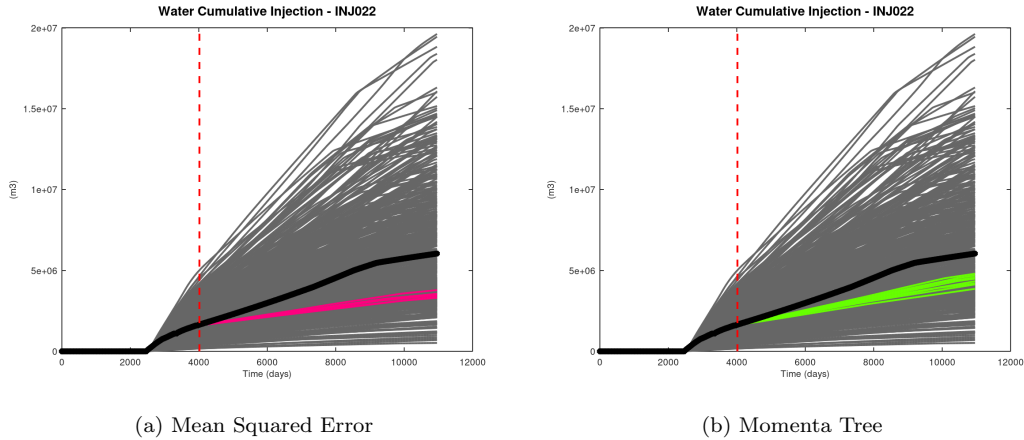
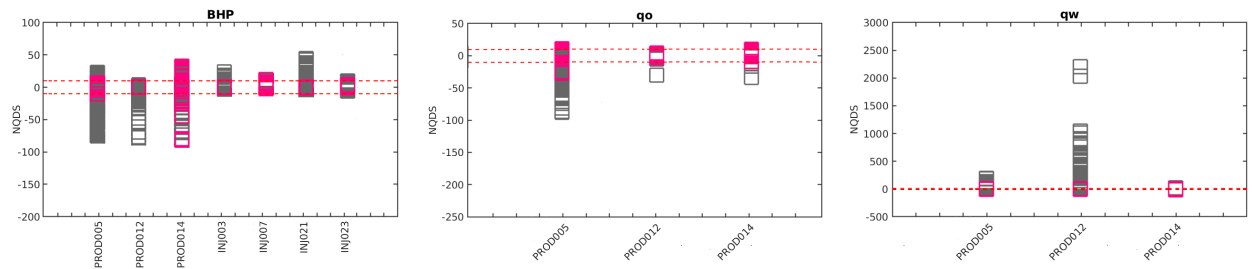
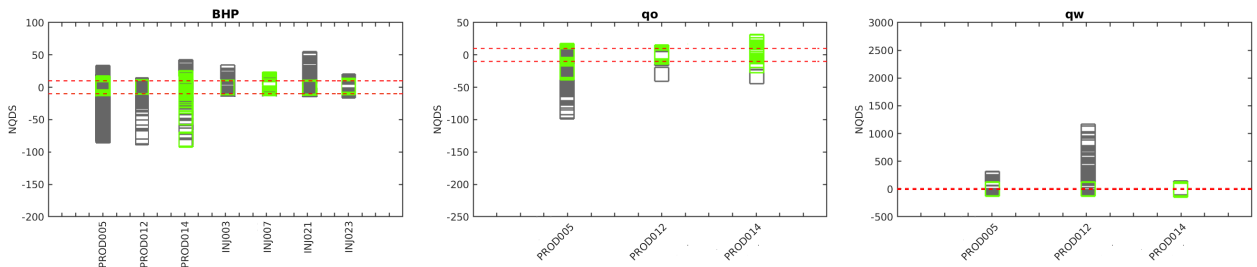


Figure 21: Local cumulative curves of forecast injections for injector 22 (INJ022). The reference is shown in black, the 490 scenarios of the final iteration in gray, the 10 best MSE-based scenarios in pink, the 10 best Momenta-Tree-based scenarios in green, and the transition between the historical and forecast period in red. When evaluating forecast behavior, the best 10 scenarios selected by the Momenta Tree metric are closer to the reference behavior than the best 10 scenarios selected by the MSE metric, with the additional advantage of permitting a comparison of data from different domains and at varying resolutions.

By observing the NQDS behavior of the wells near to the region, we see an improvement of the 10 Momenta-Tree-selected scenarios in the BHP and of producers 05 and 14. The other values do not present differences, see Figure 22.



(a) Mean Squared Error



(b) Momenta Tree

Figure 22: NQDS behavior of the wells near to the region of injector 22. The 500 models are shown in gray, the 10 MSE-selected scenarios in pink, the 10 Momenta-Tree-selected scenarios in green, and the acceptance range in red. By observing the NQDS behavior of the wells near to the region, we see an improvement of the 10 Momenta-Tree-selected scenarios in the BHP and of producers 05 and 14. The other values do not present differences.

## 6. Conclusions and Future Work

360 We have presented a new method, Momenta Tree, to explore the similarity between 4DS data and reservoir models using an image-based approach, which includes comparisons at different resolutions and in various domains. This method relies on a precise definition and representation of the similarity. **The highest-ranked scenarios selected by the Momenta Tree exhibit closer behavior to the reference case than those selected by a traditional metric, i.e., the MSE metric.**

365 We generated a benchmark that considers the common perturbations observed in 4DS images. This benchmark and a more representative case were used to analyze and evaluate the proposed method. A potential for exploring the similarity between 4DS data and reservoir models through Momenta Tree has been shown through these cases.

370 The analysis with noisy setups showed that MT strategy is much more robust than pixel-wise comparison maps correctly sorting the images in most of the cases. On the other hand, MSE-based methods are severely affected when noise is present and also when dynamic changes can happen with the images (e.g., regions appear/disappear).

The main contributions of this paper are:

- A novel strategy to compare simulated data from numerical reservoir models to observed 4DS data at different resolutions and in various domains.
- A more robust strategy of comparing images that outperforms pixel-wise comparison methods in different scenarios such as when considering different domains, dynamic environments with changes in the analyzed maps and when noise is present.
- A coherent benchmark to assess the similarity between simulated data and seismic images.

Momenta Tree's strategy is being very helpful, when we have the objective of comparing data that are in different resolutions and in different orders of magnitude, which is common to find in seismic data and data from simulation models, and mainly when we have some confidence in the interpretation of the 4D signal being able to identify the dominant effect of the domain (fluid or pressure changes). In the examples we considered hardening anomalies related to the water saturation change, due to water injection, in which the Momenta Tree is able to compare in different domains. However, different reservoirs can present anomalies due to a combination of dynamic effects (pressure variation, gas saturation variation, and other effects) which reduces the viability of employing a procedure to compare data in different domains.

In this work, we have used 3D data, 3D reservoir models and 3D volumes of seismic data. However, we have performed data comparison in 2D. This is a common practice followed in 4D data assimilation because seismic data usually has a lower vertical resolution than simulation models. Therefore, we have generated maps, by doing a vertical average, of 4D signals to compare with the corresponding vertical average of reservoir layers. For other types of reservoirs, thicker reservoirs, for instance, and 4D seismic data with higher quality, one might want to compare the whole 3D volume. In this case, our approach can be adapted to consider properties for voxels and this would represent a very promising future work.

Other future work might include, with the aid of domain experts, enhancements, such as providing more information to the users about the best paths of numerical models in the phylogenetic tree. One can also further evaluate the application using other studies, such as considering additional reservoir anomalies, that could help identify weaknesses and strengths of the current methodology.

## Acknowledgments

This work was carried out in association with the ongoing Project registered under number 20372-9 ANP the "Development of Integration between Reservoir Simulation and Seismic 4D - Phase 2 (University of Campinas [UNICAMP]/Shell Brazil/ANP), funded by Shell Brasil Petróleo Ltda. under the

405 R&D ANP levy ”Investment Commitment to Research and Development. The authors are grateful for the support of the Center of Petroleum Studies (CEPETRO-UNICAMP/Brazil), the Department of Energy (DE-FEM-UNICAMP/Brazil), the Research Group in Reservoir Simulation and Management (UNISIM-UNICAMP/Brazil), and the Energy Simulation. In addition, the authors thank Schlumberger and CMG for software licenses.

## 410 **References**

- [1] K. D. Stephen, C. Macbeth, et al., Reducing reservoir prediction uncertainty using seismic history matching, in: SPE Europec/EAGE Annual Conference, Society of Petroleum Engineers, 2006, pp. 1–9.
- [2] A. Davolio, C. Maschio, D. J. Schiozer, et al., Local history matching using 4d seismic data and multiple models combination, in: SPE Europec/EAGE Annual Conference, Society of Petroleum Engineers, 2013, pp. 1–10.
- [3] O. Gosselin, S. Aanonsen, I. Aavatsmark, A. Cominelli, R. Gonard, M. Kolasinski, F. Ferdinandi, L. Kovacic, K. Neylon, et al., History matching using time-lapse seismic (huts), in: SPE Annual Technical Conference and Exhibition, Society of Petroleum Engineers, 2003, pp. 1–15.
- 420 [4] P. Berthet, L. Barends, P. Prat, History matching of production data and 4d seismic data on girassol field, in: SPE Europec/EAGE Annual Conference, 2008, pp. 1–5.
- [5] E. Tolstukhin, B. Lyngnes, H. H. Sudan, et al., Ekofisk 4d seismic-seismic history matching workflow, in: SPE Europec/EAGE Annual Conference, Society of Petroleum Engineers, 2012, pp. 1–14.
- 425 [6] A. A. Emerick, Analysis of the performance of ensemble-based assimilation of production and seismic data, *Journal of Petroleum Science and Engineering* 139 (2016) 219–239.
- [7] J.-A. Skjervheim, G. Evensen, S. I. Aanonsen, B. O. Ruud, T.-A. Johansen, et al., Incorporating 4d seismic data in reservoir simulation models using ensemble kalman filter, in: SPE Annual Technical Conference and Exhibition, Society of Petroleum Engineers, 2005, pp. 1–10.
- 430 [8] E. Tillier, S. Da Veiga, R. Derfoul, Appropriate formulation of the objective function for the history matching of seismic attributes, *Computers & Geosciences* 51 (2013) 64–73.
- [9] R. Derfoul, S. Da Veiga, C. Gout, C. Le Guyader, E. Tillier, Image processing tools for better incorporation of 4d seismic data into reservoir models, *Journal of Computational and Applied Mathematics* 240 (2013) 111–122.

- 435 [10] R. Chassagne, D. Obidegwu, J. Dambrine, C. MacBeth, Binary 4d seismic history matching, a metric study, *Computers & Geosciences* 96 (2016) 159–172.
- [11] S. Zahra, H. Hamdi, R. C. R. Mota, M. C. Sousa, F. Maurer, A visual analytics framework for exploring uncertainties in reservoir models, in: *International Joint Conference on Computer Vision, Imaging and Computer Graphics Theory and Applications*, SciTePress, 2018, pp. 74–84.
- 440 [12] D. S. Oliver, Y. Chen, Recent progress on reservoir history matching: a review, *Computational Geosciences* 15 (1) (2011) 185–221.
- [13] S. Danaei, G. M. S. Neto, D. J. Schiozer, A. Davolio, Using petro-elastic proxy model to integrate 4d seismic in ensemble based data assimilation, *Journal of Petroleum Science and Engineering* (2020) 107457.
- 445 [14] Z. Yin, T. Feng, C. MacBeth, Fast assimilation of frequently acquired 4d seismic data for reservoir history matching, *Computers & Geosciences* 128 (2019) 30–40.
- [15] Y. Zhang, O. Leeuwenburgh, Image-oriented distance parameterization for ensemble-based seismic history matching, *Computational Geosciences* 21 (4) (2017) 713–731.
- [16] A. Davolio, D. J. Schiozer, Probabilistic seismic history matching using binary images, *Journal of Geophysics and Engineering* 15 (1) (2018) 261.
- 450 [17] S. Suzuki, J. Caers, A distance-based prior model parameterization for constraining solutions of spatial inverse problems, *Mathematical geosciences* 40 (4) (2008) 445–469.
- [18] C. Scheidt, J. Caers, Representing spatial uncertainty using distances and kernels, *Mathematical Geosciences* 41 (4) (2009) 397.
- 455 [19] S. Rojas, V. Demyanov, M. Christie, D. Arnold, Controlling the sedimentological realism of deltaic reservoir models by the use of intelligent sedimentological prior information, *First Break* 32 (10) (2014) 69–72.
- [20] L. Jin, D. Weber, P. van den Hoek, F. O. Alpak, C. Pirmez, 4d seismic history matching using information from the flooded zone, *First Break* 30 (7) (2012) 55–60.
- 460 [21] D. Obidegwu, R. Chassagne, C. MacBeth, et al., Seismic assisted history matching using binary image matching, in: *SPE Europec, Society of Petroleum Engineers*, 2015, pp. 1–22.
- [22] C. Zhu, G. Zhang, P. Lu, L. Meng, X. Ji, Benchmark modeling of the sleipner co 2 plume: Calibration to seismic data for the uppermost layer and model sensitivity analysis, *International Journal of Greenhouse Gas Control* 43 (2015) 233–246.

- 465 [23] H. Jeong, S. Srinivasan, Fast selection of geologic models honoring co<sub>2</sub> plume monitoring data using hausdorff distance and scaled connectivity analysis, *International Journal of Greenhouse Gas Control* 59 (2017) 40–57.
- [24] S. Rahim, Z. Li, Reservoir geological uncertainty reduction: an optimization-based method using multiple static measures, *Mathematical Geosciences* 47 (4) (2015) 373–396.
- 470 [25] C. Scheidt, J. Caers, Bootstrap confidence intervals for reservoir model selection techniques, *Computational Geosciences* 14 (2) (2010) 369–382.
- [26] X. Luo, A. S. Stordal, R. J. Lorentzen, G. Naevdal, et al., Iterative ensemble smoother as an approximate solution to a regularized minimum-average-cost problem: Theory and applications, *SPE Journal* 20 (05) (2015) 962–982.
- 475 [27] X. Luo, T. Bhakta, M. Jakobsen, G. Naevdal, Efficient big data assimilation through sparse representation: A 3d benchmark case study in petroleum engineering, *PLOS ONE* 13 (7) (2018) 1–32.
- [28] J. Ghosh, A. Strehl, Similarity-based text clustering: a comparative study, in: *Grouping Multi-dimensional Data*, Springer, 2006, pp. 73–97.
- 480 [29] A. M. Cuadros, F. V. Paulovich, R. Minghim, G. P. Telles, Point placement by phylogenetic trees and its application to visual analysis of document collections, in: *IEEE Symposium on Visual Analytics Science and Technology*, 2007, pp. 99–106.
- [30] D. Knuth, *The Art of Computer Programming: Fundamental algorithms*, Addison-Wesley series in computer science and information processing, Addison-Wesley, 1968.
- 485 URL <https://books.google.com.br/books?id=9W2HtQEACAAJ>
- [31] M. Santos, J. de Lope, et al., Orthogonal variant moments features in image analysis, *Information Sciences* 180 (6) (2010) 846–860.
- [32] R. C. Gonzalez, R. E. Woods, S. L. Eddins, et al., *Digital image processing using MATLAB.*, Vol. 624, Pearson-Prentice-Hall Upper Saddle River, New Jersey, 2004.
- 490 [33] D. C. Anastasiu, G. Karypis, Efficient identification of tanimoto nearest neighbors, in: *2016 IEEE International Conference on Data Science and Advanced Analytics (DSAA)*, IEEE, 2016, pp. 156–165.
- [34] N. Saitou, M. Nei, The neighbor-joining method: a new method for reconstructing phylogenetic trees., *Molecular Biology and Evolution* 4 (4) (1987) 406–425.

- 495 [35] M. Lungu, K. Xu, Biomedical information visualization, in: Human-centered visualization environments, Springer, 2007, pp. 311–342.
- [36] G. D. Avansi, D. J. Schiozer, Unisim-i: synthetic model for reservoir development and management applications, International Journal of Modeling and Simulation for the Petroleum Industry 9 (1).
- 500 [37] D. Alfred, S. Atan, J. G. Hamman, D. H. Caldwell, et al., Petro-elastic models-how many and at what scale?, in: Europec/EAGE Conference and Exhibition, Society of Petroleum Engineers, 2008, pp. 1–9.
- [38] S. Lancaster, D. Whitcombe, Fast-track coloured inversion: 70th annual international meeting, seg, expanded abstracts, 1572–1575 (2000).
- 505 [39] A. Davolio, D. Schiozer, A proper data comparison for seismic history matching processes, in: SPE Europec featured at 81st EAGE Conference and Exhibition, 2019, pp. 1–11.
- [40] R. M. Souza, Quantitative integration of 4d seismic and production data for saturation estimation and fluid-flow model assessment, Ph.D. thesis, University of Western Australia (2017).

### Computer Code Availability

510 The code of the Momenta Tree methodology is contained in the following link: <https://github.com/aurea-soriano/MomentaTreeSimilarity.git>. The code was developed in Python using 64-bit Python 2.7.6 and developed in PyDev 4.11 IDE, making use of the NumPy 1.15.2, and Scikit 0.17.